Accurate computation of chemical contrast in field ion microscopy

Shalini Bhatt, Shyam Katnagallu, Jörg Neugebauer, and Christoph Freysoldt
Max-Planck-Institut für Eisenforschung GmbH, 40227 Düsseldorf, Germany

(Received 20 December 2022; revised 25 April 2023; accepted 2 June 2023; published 16 June 2023)

We present a computational approach to simulate local contrast observed in field ion microscopy (FIM). It is based on density-functional theory utilizing the Tersoff-Hamann approach as done in scanning tunneling microscopy (STM). A key requirement is the highly accurate computation of the surface states' wave-function tails. To refine the Kohn-Sham states from standard iterative global solvers we introduce and discuss the EXtrapolation of Tails via Reverse integration Algorithm (EXTRA). The decaying tails are obtained by reverse integration (from outside in) using a Numerov-like algorithm. The starting conditions are then iteratively adapted to match the values of plane-wave Kohn-Sham wave functions close to the surface. We demonstrate the performance of the proposed algorithm by analyzing and showing the chemical contrast for Ta, W, and Re at Ni surface.

DOI: 10.1103/PhysRevB.107.235413

I. INTRODUCTION

Field ion microscopy (FIM) was the first microscopy technique to image individual atoms on a metal surface with atomic spatial resolution [1,2]. An imaging gas (e.g., He, Ne) is ionized above the surface of a nanosharp needle-shaped specimen (end diameter <100 nm) subject to a high electric field of 10^{10} V/m. The ions are then accelerated along the field lines on to a two-dimensional detector to produce an image of the tip surface magnified [3] by a factor of 10^7. While FIM has been mostly replaced by scanning tunneling microscopy [4], atomic force microscopy, and similar scanning probe techniques [5] for surface characterization, there has been a recent resurgence when combined with field evaporation. Field evaporation refers to the process by which electric fields induce the removal of atoms from needle-shaped specimens. This technique enables FIM to extend its capabilities to provide atomically resolved 3D characterization. The ions produced by field evaporation can be identified using time-of-flight spectrometry, which also adds analytical capabilities to FIM. 3D-FIM [6–9] and aFIM [10,11] are state-of-the-art techniques that utilize these capabilities to analytically image crystallographic features with atomic resolution in three dimensions besides electron tomography [12]. Both 3D-FIM and aFIM are able to provide quasi-analytical images at atomic scale not only for pure materials (Fe,W) but also for complex samples such as FeBSi [13,14]. They were recently used to provide insights into crystallographic defects such as vacancies [8,15,16], dislocations and voids [10,17]. Traditional FIM is also now used for analyzing reaction kinetics of various crystallographic facets of Rh for catalytic CO oxidation. [18]. Despite the resurgence of FIM based techniques, the quantitative interpretations of imaging contrast enabled by theory have been sparse [19]. Numerous studies have focused on understanding the image contrast in field ion images from a theoretical perspective [20–28], but a widely applicable framework to predict and interpret FIM contrast has not yet emerged.

Under best imaging field conditions, the local imaging contrast is dominated by the ionization probability at 5–10 Å above the surface [29]. Ionization near the surface requires an electron transfer from the gas atom into an empty surface state, see Fig. 1. Without an electrostatic field, this would be energetically impossible since the ionization level of the imaging gas ($\approx$15–25 eV) exceeds the work function ($\approx$3–6 eV for most metals). The electric field provides the required voltage drop to overcome this difference and thereby enables electron tunneling when the gas atom is beyond a critical distance from the surface. For tunneling into further energetically higher states, the tunneling distance would be accordingly larger.

Unfortunately, previous analytic theories of field ionization have focused on simplified scenarios. Forbes concluded in his 2003 review of field ionization theory [27]: "A problem is that the complexity of the field-ion imaging situation is so great that it is well nigh impossible to formulate any valid detailed numerical theory. There are image-contrast problems to be solved, certainly with some alloy materials. But the problem more likely lies in the nature of the electronic structure of the substrate, and how this influences local fields above individual atoms."

With the present paper, we aim at closing this gap by a general quantitative framework based on density-functional theory (DFT). For tunneling, we adapt the well-known the Tersoff-Hamann approach used in STM [30], that links tunneling probability to the local density of states (DOS), which in turn is computed from the DFT Kohn-Sham wave functions. Preliminary work by us [10,11] presented elements of this

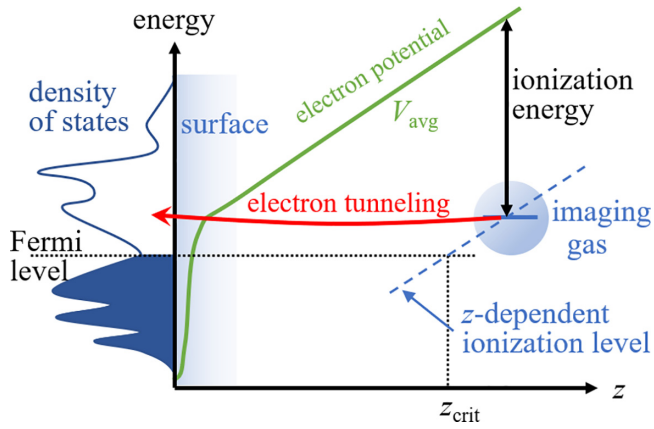

FIG. 1. Schematic diagram of field ionization. Electrons tunnel from the imaging gas (right) to an energetically aligned empty surface state (left). The plane-averaged electron potential V_{avg} is marked by a green line. The ionization level (dashed line) and hence the energy of tunneling varies with distance z due to the electric field. For detailed discussion see Eq. (2). Below the critical distance z_{crit}, the ionization level is below the Fermi level and tunneling cannot take place.

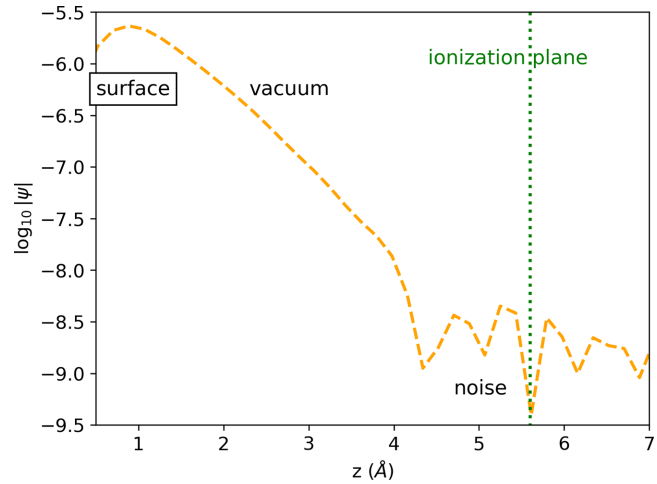

FIG. 2. Typical evolution of numerical wave functions on top of Ta in a Ni(012) surface in the presence of an electric field as obtained from a standard DFT code. The decay behavior of the wave function (orange curve) is shown for an eigenvalue at the Fermi level. For FIM image contrast, ψ is needed at the ionization plane.

framework, but neither provided a complete, general treatment of the physical picture nor of the specific computational challenges.

In our previous paper [10], we applied the Tersoff-Hamann approximation in DFT simulations in presence of a field to explain the brighter appearance of Re atoms during FIM imaging of a Ni-Re alloy, focusing on states right above the Fermi level. While such a selective approach explained the chemical contrast in this case, the numerical accuracy in other cases emerged as a critical issue. In our recent paper on Ta-doped Ni [11], we proposed that Ta-induced empty states 1–3 eV above the Fermi level are responsible for the brightness contrast, but failed to quantify the interplay of distance and tunneling energy due to numerical noise of DFT wave functions.

The computational challenge in these calculations is that the high electric field leads to a very fast decay of wave functions into the vacuum. In many cases, we found that the accuracy of wave functions from standard DFT is insufficient to make quantitative predictions for FIM, as sketched in Fig. 2. The standard wave-function optimization algorithms implemented in plane-wave DFT codes are based on the Rayleigh-Ritz method of minimizing the global norm of the residue [31]. This implies that the highest magnitude in the wave function determines the global algorithm's notion of "large" and "small". Hence, they give the best relative accuracy where the wave function amplitude is large. On the downside, in areas where the wave function is small in magnitude, the relative error between the approximate solution and the exact solution can become excessively large even if the total residue is at the numerical limit. The electrostatic field present in FIM further leads to a strong, nonexponential decay of wave functions and they run into a regime where noise dominates. Unfortunately, this is exactly the region of space where the wave functions are needed to apply the Tersoff-Hamann approximation for FIM. We considered using an expansion in smooth atom-centered orbitals (or any other type of predefined basis functions "attached" to the surface), but found that this is not an option because the rising, nontrivial vacuum potential at hand induces a decay behavior that deviates from the assumed shape of the basis functions' tails (e.g., Gaussian, exponential).

The solution presented in this paper is to recompute the tails of the wave functions with an algorithm that works at the local scale. More precisely, we develop an algorithm that is local with respect to the dominant direction for scale (in the following, z), i.e., away from the slab surface. For this, we assume that the eigenvalues ϵ_i and corresponding eigenfunctions $\psi_i(\mathbf{r})$ close to the slab have been reliably computed. Then, the task is to integrate the underlying second-order differential equation, i.e., the Kohn-Sham equation from this trusted region along the z direction.

The rest of this article is organized as follows. In Sec. II we explain how DFT in combination with Tersoff-Hamann tunneling theory enables the prediction of FIM contrast. In Sec. III, we will present our tail extrapolation scheme and show that it is robust even if the wave function amplitude varies over several orders of magnitude along the direction of integration. In Sec. IV we apply the algorithm to a prototype surface, namely the Ni(012) containing substitutional atoms (Ta, W, Re), and show that we can successfully reproduce the enhanced brightness observed in experiment [11,13].

II. DFT-BASED THEORY OF FIM CONTRAST

In the present paper, DFT was performed in the plane-wave PAW formalism with the SPHInX code [32] using the Perdew-Burke-Ernzerhof (PBE) exchange-correlation functional [33] The calculation was spin-polarized with colinear spin and produced a ferromagnetic state. The Ni (012) surface was modeled in the repeated slab approach with nine atomic layers at the theoretical lattice constant (3.465 Å) and a vacuum separation of 17.5 Å. An electric field of 40 V/nm was included via the generalized dipole correction

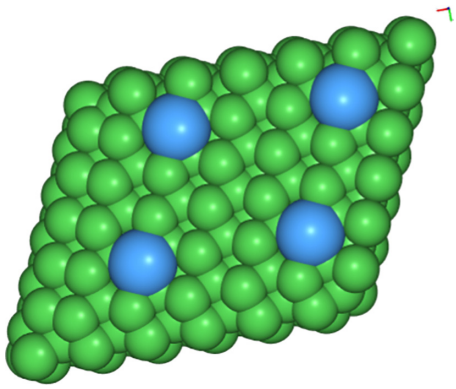

FIG. 3. Top view of Ta-Ni(012) where Ta atoms (blue) are surrounded by Ni atoms (green). The 3×3 surface cell has been repeated in both directions for clarity.

[34]. Metal substitution (Ta, W, Re) at the surface was modeled in a 3×3 surface unit cell, i.e., with nine surface atoms as shown in Fig. 3. The six topmost layers were relaxed via quasi-Newton optimization with a redundant internal coordinated Hessian fitted on the fly [35] until the forces were below 0.015 eV/Å. For the structure optimization, an offset $2 \times 3 \times 1$ **k**-point sampling was used, equivalent to a **k**-point spacing of 0.13 bohr^{-1}. For computing the wave functions in the FIM contrast simulation, the **k**-point density in the plane was doubled ($4 \times 6 \times 1$).

To simulate the FIM imaging contrast due to the electronic structure of the surface, we build on an analogy to scanning tunneling microscopy (STM). Both STM and FIM use electron tunneling for forming an image of a solid surface. STM relies on electron tunneling between a sample surface and probe tip when a small voltage is applied between them. In their ground-breaking paper [30], Tersoff and Hamann found the tunneling current in STM to be proportional to the surface local density of states (DOS) near the Fermi level at the position of the STM tip. Their derivation equally applies when the spherical tip is replaced by a single atom.

There are, however, important differences between STM and FIM when it comes to the relevant spatial positions, involved states, and the role of the applied voltage: In STM, the tip position and the voltage between the tip and the scanned surface can be controlled. The main role of the voltage is to shift the Fermi level of the tip relative to one of the surface. Explicit field-induced changes are neglected. This is well justified for voltages of a few tenths of an eV, applied over a distance on the order of 1 nm. The tunneling current then occurs between states lying between the two Fermi levels. As the tip is retracted from the surface, the tunneling current decays exponentially.

In contrast, tunneling in FIM occurs between a single electronic level of the imaging gas (namely the highest occupied one) and a suitably aligned empty state of the surface, see Fig. 1. The externally applied field between the (positively charged) surface and the (negative) counterelectrode far away makes the energy of the imaging gas orbital rise relative to the surface's electronic structure as the distance to the surface increases, as indicated by the dashed line in Fig. 1. The further out the atom is, the higher the orbital energy. Thus, instead of tunneling from a fixed position across a range of states defined by the applied voltage as in STM, tunneling in FIM occurs over a range of possible positions, and in each of these positions to those few surface states that happen to be energetically degenerate with the ionization level of the atom at this position. The range of accessible states is then not defined from the applied voltage. Rather, high-lying states give negligible contributions because the tunneling probability rapidly decays as the distance (and thus the orbital energy) increases, which implicitly imposes an upper limit of relevance.

Moreover, the field strength in FIM (a few ten V/nm) is higher than in STM, so explicit fields must be considered in simulations [10,34]. The field not only impacts the charge distribution across the surface and the relaxation of surface atoms due to Maxwell stress [34], but also enhances the wave function decay. In consequence, the limits of numerical accuracy for the tails of the wave functions become a critical issue.

Let us now consider how this model of FIM contrast develops into a computational scheme. The partial DOS at energy E and position $\mathbf{r}$ is given by

$$\rho(\mathbf{r}, E) = \sum_{i\sigma\mathbf{k}} w_{\mathbf{k}} |\psi_{i\sigma\mathbf{k}}(\mathbf{r})|^2 \delta(E - \epsilon_{i\sigma\mathbf{k}}) \tag{1}$$

for state index i and spin index σ. $w_{\mathbf{k}}$ denotes the **k**-point weight. To turn this into a two-dimensional FIM contrast map, we impose energy conservation for the tunneling process, i.e.,

$$E = \epsilon_{i\sigma\mathbf{k}} = V_{\text{avg}}(x, y, z) - I, \tag{2}$$

where I is the (positive) ionization energy of the imaging gas. V_{avg} is the average potential that the imaging gas atom experiences. For simplicity we assume here that $V_{\text{avg}}(x, y, z) \approx \overline{V}(z)$, the planar average of the potential along the xy plane parallel to the surface. This energy conservation condition requires tunneling into higher-lying states to occur further away from the surface. Due to the rapid, overexponential decay of wave functions, the overall contribution of higher-lying states is effectively dampened. This relieves us from making *ad hoc* assumptions on which states are relevant for tunneling. In practice, we truncate the energy range at ≈5 eV above the Fermi level. We verified that the contribution of the highest of these states to the overall intensity is negligible. Combining Eqs. (1) and (2), the FIM contrast is proportional to

$$F(x, y) = \sum_{i\sigma\mathbf{k}} w_{\mathbf{k}} |\psi_{i\mathbf{k}}(x, y, z_{i\sigma\mathbf{k},I})|^2 \tag{3}$$

where the sum runs over states above the Fermi level. The evaluation height $z_{i\sigma\mathbf{k},I}$ is implicitly defined by

$$\overline{V}(z_{i\sigma\mathbf{k},I}) = \epsilon_{i\sigma\mathbf{k}} + I. \tag{4}$$

In practice, we run a search on the discrete z grid, and then linearly interpolate the DOS between the discrete z points. As the varying contribution of states at different energies is controlled by their decay behavior, we strongly rely on an accurate description of the wave function tails. The tails produced by the standard wave function optimizers (Rayleigh-Ritz minimization) turn out to be insufficient, as they are dominated by noise in the region of interest, i.e., at $z_{i\sigma\mathbf{k},I}$. In the following section, we therefore present an algorithm to recompute these tails, by numerically integrating the underlying partial differential equation in space.

III. EXTRAPOLATION OF TAIL VIA REVERSE INTEGRATION ALGORITHM (EXTRA)

A. Reverse integration

In DFT, the Kohn-Sham equation reads [36]

$$\left(-\tfrac{1}{2}\nabla + V_{\text{eff}}(\mathbf{r})\right)\psi_i(\mathbf{r}) = \epsilon_i \psi_i(\mathbf{r}) \tag{5}$$

using Hartree atomic units ($\hbar = 1$, $m_e = 1$, $4\pi\epsilon_0 = 1$). The effective potential is obtained as

$$V_{\text{eff}} = V_{\text{ext}} + V_{\text{H}} + V_{\text{xc}}. \tag{6}$$

The external potential V_{ext} defines the Coulomb interaction between an electron and the collection of atomic nuclei. The Hartree potential V_{H} describes the classical Coulomb repulsion between the electrons, and the exchange-correlation potential V_{xc} encompasses quantum mechanical corrections. In common density-based approximations (e.g., LDA, GGA, meta-GGA), V_{xc} depends on the local density and vanishes as the density becomes zero. The vacuum potential is therefore dominated by the electrostatic potential $V_{\text{ext}} + V_{\text{H}}$.

Rewriting Eq. (5) as

$$\frac{1}{2}\frac{\partial^2}{\partial z^2}\psi_i(\mathbf{r}) = \left\{-\frac{1}{2}\left(\frac{\partial^2}{\partial x^2} + \frac{\partial^2}{\partial y^2}\right) + V_{\text{eff}}(\mathbf{r}) - \epsilon_i\right\}\psi_i(\mathbf{r}) \tag{7}$$

provides the basis to numerically integrate the wave function ψ_i along the z direction. For the sake of readability, we will omit the state index i from the equations in the following.

It is well known from the theory of second-order differential equations in one dimension (1D) that there are two linearly independent solutions. In our case, a decaying and a rising solution are possible. In forward integration, the decaying solution is always challenging to compute because numerical noise (e.g., rounding errors due to the finite precision) can produce a small contribution of the rising solution, which then grows as the algorithm proceeds and ultimately dominates.

To circumvent this problem, one can reverse the direction of integration: by starting deep in the vacuum and integrating towards the surface, the desired solution is growing in magnitude and thus can be easily computed. In consequence, the extrapolation problem is turned into a problem of choosing starting conditions such that the integrated tail solution matches the values of the global optimization near the surface, in our case at the matching plane $z = z_{\text{match}}$.

Before we come to the integration algorithm, let us briefly review the key properties of the effective potential. In vacuum, where the density becomes negligibly small, the electrostatic part becomes dominant and V_{xc} vanishes. Hence, it is interesting to understand how the electrostatic potential develops far away from the surface. For this, one can apply a Fourier transform in the xy plane [with wave vector $\mathbf{k} = (k_x, k_y)$] to a "mixed-space" representation $V(\mathbf{k}, z)$. As shown in Appendix A, the xy-averaged electrostatic potential is constant or diverges linearly along z, while the lateral potential variations decay exponentially. Hence, beyond a certain point, the xy-averaged potential will strongly dominate the evolution of the wave functions along z. We, therefore, decompose the potential

$$V(x, y, z) = \overline{V}(z) + \delta V(x, y, z) \tag{8}$$

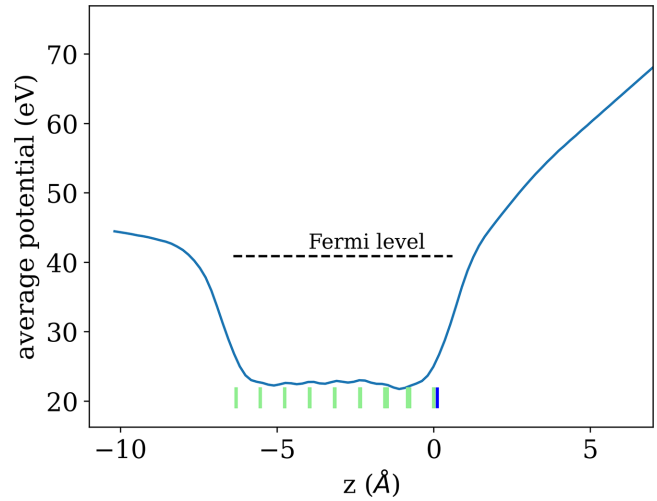

FIG. 4. The effective potential along z averaged over xy plane of a charged Ta-Ni(012) slab with nine atomic layers as indicated by vertical lines (green: Ni, blue: Ta). An electric field of 40 V/nm is applied at the top side

into the average potential $\overline{V}$ for $k_x = k_y = 0$ component and the lateral variation δV for $|\mathbf{k}| > 0$. Figure 4 shows the average potential obtained from DFT calculations discussed in Sec. IV.

B. Overview of tail extrapolation

In our algorithm, we split the space above the surface into three regions, named regions I, II, and III from outside in, as shown schematically in Fig. 5. Region III, closest to the surface, is where the DFT program's global solver provides sufficiently accurate numerical wave functions and hence does not require additional optimization. For simplicity, we define region III below a plane parallel to the surface, at height z_{match}. Region I is far away from the slab, where the lateral variations of the potential are negligible. As shown in Sec. III C, this simplification renders the Kohn-Sham equation separable in the mixed space within region I, and allows us to use 1D Numerov integration along z as an efficient and accurate algorithm to compute wave-function tails. Closer to the slab, in region II, lateral variations in the potential become important and the 1D Numerov would be inaccurate. We therefore generalized the Numerov algorithm to three dimensions (see Appendix B) to perform integrations in region II. In Sec. III D we show that this must be combined with Fourier filtering in mixed space to ensure robustness over many orders of magnitude for the wave-function amplitude. In practice, our Fourier filtering can be seen as introducing a curved boundary in mixed $(\mathbf{k}, z)$ space between region I and region II.

The key task to ensure a coherent wave function across all three regions is to make the separately computed wave functions match at the region I/region II and the region II/region III boundaries, respectively. For the former, this is readily achieved by rescaling, see Sec. III C below. For the latter, where the region III wave functions are authoritative, we employ an iterative procedure summarized in Sec. III E. As the I/II boundary values serve as starting values for region II

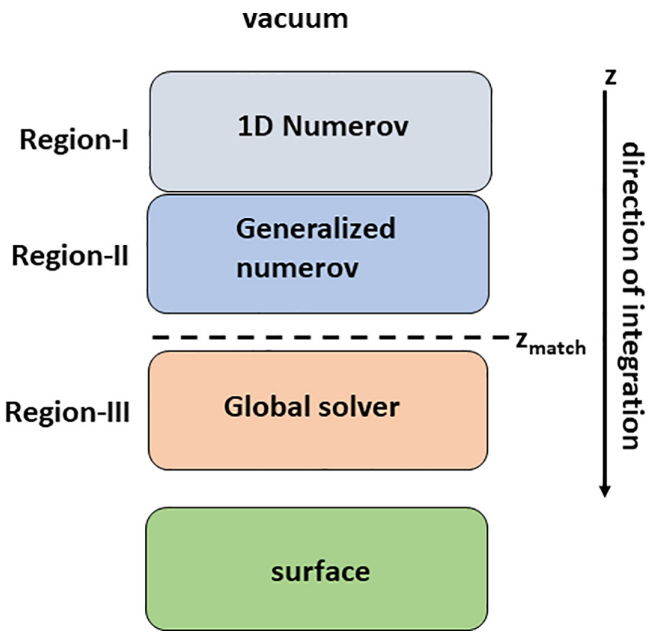

FIG. 5. Algorithm applied to the various regions above the surface. The reverse integration in z starts from the top to the bottom (z_{match}). In region I the 1D Numerov solution is computed. In region II the EXTRA algorithm is applied. Region III contains the unmodified plane-wave wave functions obtained from the global solver (plane-wave DFT code).

reverse integration towards region III, we vary these boundary values to minimize mismatch at the II/III boundary. The combined approach, i.e., 1D integration in region I (Sec. III C), Fourier-filtered generalized Numerov integration in region II (Sec. III D), and the iterative procedure for determining the I/II boundary values as the key unknowns in wave-function matching (Sec. III E), is termed EXTRA (extrapolation of tails via reverse integration algorithm).

C. Region I: 1D Numerov integration in mixed space

Deep in vacuum, δV becomes negligible, and Eq. (8) reduces to

$$V(x, y, z) \approx \overline{V}(z). \tag{9}$$

Within this approximation, an in-plane Fourier transform makes the Kohn-Sham equation, Eq. (7), separable in $\mathbf{k}$ and z, i.e., in mixed space

$$\frac{1}{2}\frac{\partial^2 \psi(\mathbf{k}, z)}{\partial z^2} = \left\{\frac{1}{2}|\mathbf{k}|^2 + \overline{V}(z) - \epsilon\right\}\psi(\mathbf{k}, z) \tag{10}$$

with both growing and decaying solutions if $\epsilon < \overline{V}(z)$ for all z. For recomputing the decaying tails, 1D Numerov is a feasible algorithm [37,38]. For this, one performs reverse Numerov integration, starting deep in the vacuum with arbitrary non-vanishing initial values, and rescales the intermediate solution such that it matches a given value $\psi(\mathbf{k}, z_{\text{start}})$ at the boundary z_{start} between regions I and II.

The Numerov method is a finite difference method that calculates the shape of the wave function by integrating step-by-step along a grid. The one-dimensional Schrödinger equation is solved using Numerov algorithm [39] in form of

$$\psi_{n+1} = \frac{2\left(1 - \frac{5}{12}h^2k_n^2\right)\psi_n - \left(1 + \frac{1}{12}h^2k_{n-1}^2\right)\psi_{n-1}}{1 + \frac{1}{12}h^2k_{n+1}^2} \tag{11}$$

where

$$k_n^2 = 2\epsilon - 2\overline{V}(z_n) - |\mathbf{k}|^2. \tag{12}$$

There are different variants of Numerov [40,41] developed in the past for the approximate solution of Schrödinger equation. The discretization error of the Numerov algorithm is $\mathcal{O}(h^6)$.

The numerical accuracy of the Numerov algorithm for rising solutions over many orders of magnitude arises from the locality: only the previous two values are needed, and these lie at a very similar magnitude. Uncorrelated numerical round-off errors cannot grow faster than the exact solution, because they either are proportional to the desired solution or belong to the linearly independent, decaying solution. This also ensures that starting from arbitrary values will always converge towards the rising solution after a warmup phase.

D. Region II: Fourier-filtered generalized Numerov integration

1. *Generalized Numerov algorithm*

In order to numerically integrate the 3D Schrödinger equation along the z direction, we propose a generalized Numerov algorithm given in Appendix B. The working equation is [cf. Eq. (B6)]

$$\begin{aligned}\left[1 + \tfrac{1}{6}h^2\left\{\epsilon - \hat{V}(z_{n+1})\right\}\right]\psi_{n+1} \\ = 2\left[1 - \tfrac{5}{6}h^2\left\{\epsilon - \hat{V}(z_n)\right\}\right]\psi_n \\ -\left[1 + \tfrac{1}{6}h^2\left\{\epsilon - \hat{V}(z_{n-1})\right\}\right]\psi_{n-1}.\end{aligned} \tag{13}$$

Equation (13) represents an in-plane partial differential equation [with linear operator $\hat{V}(z)$] for ψ_{n+1} with a known right-hand side that depends on the values for the two previous steps z_n and z_{n-1}. By solving this differential equation numerically using a standard (plane-global) iterative algorithm, one can stepwise proceed along the z direction. The in-plane kinetic operator is computed in mixed space, while the potential is applied in real space, using fast Fourier transforms to switch between these two spaces. To solve the discretized differential equation, we employ the root finding solver of the Scipy optimization module [42] (scipy.optimize.root) with Krylov subspace iterations [43] and a numerical approximate inverse Jacobian.

The key advantage of this procedure is that the numerical solver of the in-plane equation must only deal with scale variations within the plane, while the huge changes in magnitude along the z direction are taken care of by the explicit iteration $(\psi_{n-1}, \psi_n) \to \psi_{n+1}$.

2. *High-frequency noise issues with unfiltered generalized Numerov*

We have tested the generalized Numerov numerical integration in the reverse direction in a region near the surface

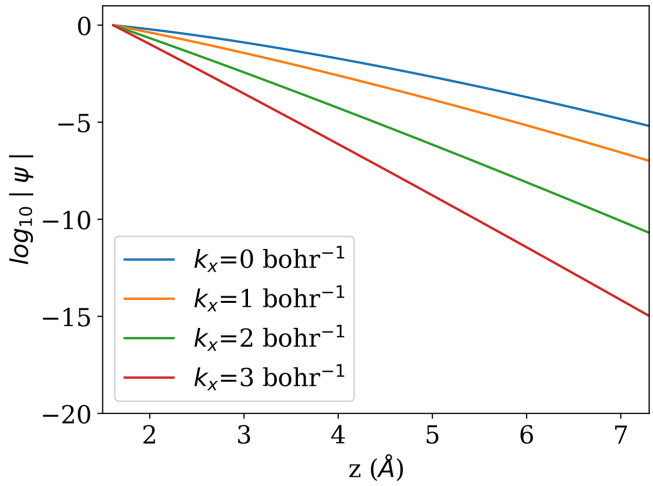

FIG. 6. 1D Numerov wave-function magnitude as a function of surface-ion distance z using the potential shown in Fig. 4. The topmost nuclear positions are located at $z = 0$. The decay rate depends on in-plane Fourier components k_x. The wave functions are calculated for an eigenvalue at the Fermi level and normalized with respect to $z_{\text{match}} = 1.7$ Å.

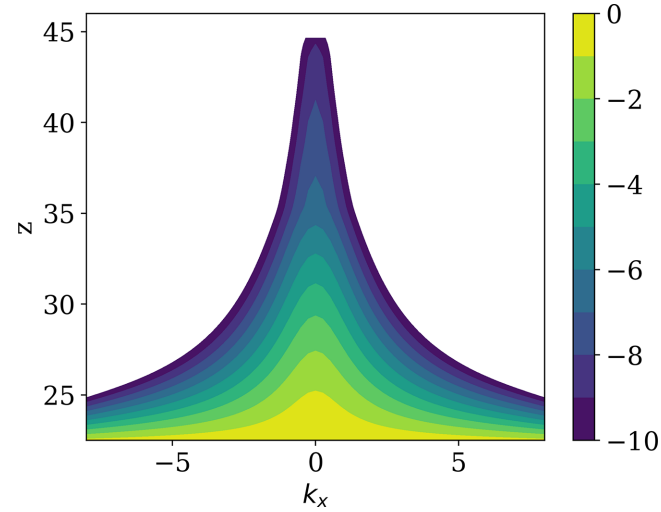

FIG. 7. Iso-magnitude contours of wave functions above Ta-Ni(012) plotted in mixed space. The wave functions were generated from 1D Numerov using the average potential (see Fig. 4), and were normalized with respect to $z_{\text{match}} = 22$ bohr.

where the global solver provides a nicely decaying reference solution discussed in the Supplemental Material [44]

Generalized Numerov is stable against numerical noise from the unwanted solution (i.e., the exponential rising solution into vacuum). Unfortunately, when integrating towards the surface, it produces a rapid increase of contributions from high-frequency Fourier components in the plane that are absent from the reference solution. This is not a failure in principle, as we can expect from the separable approximation, Eq. (A2) that in-plane frequency coefficients for high $\mathbf{k}$ values have steeper slopes along z compared to the low-frequency ones as shown in Fig. 6. Yet, this makes the generalized Numerov algorithm of Appendix B sensitive to high-frequency noise. The reason behind the discrepancy is visualized in Fig. 7, which illustrates how the wave-function magnitude develops for different k_x values.

As shown in Fig. 7, iso-magnitude contours in mixed (k_x, k_y, z) space are not parallel to the (k_x, k_y) plane. In consequence, we find that it is not sufficient to find an algorithm that has a local scale in only z, but actually, one that respects the local scale in (k_x, k_y, z). To circumvent the above issue, we additionally employ a z-dependent Fourier filtering in the xy plane. The challenge is to distinguish between noise and the true signal. Fortunately, for each mixed-space coefficient, we can estimate the expected magnitude relative to the matching plane from the 1D separable equation, Eq. (10). We can use this to make a Fourier-filtering at "equal magnitude".

3. *The iso-magnitude boundary for regions I/II*

At the boundary between region II/region III high-frequency Fourier components obtained by the generalized Numerov algorithm grow rapidly and need to be filtered out. To do this we make the boundary k dependent using the iso-magnitude condition

$$\psi_{1d}(\mathbf{k}, z_{\text{start}}(\mathbf{k}))/\psi_{1d}(\mathbf{k}, z_{\text{match}}) = \eta \qquad (14)$$

where η defines the magnitude threshold. Equation (14) defines a finite $z_{\text{start}}(\mathbf{k})$ beyond which the coefficients can be effectively ignored (set to zero) for the generalized Numerov step as shown in Fig. 7. The choice of η is not overly problematic in practice. We have successfully employed values of 10^{-6}, 10^{-8}, and even 10^{-20} and observed negligible differences between the results. If η is chosen too small, high-frequency noise occurs. If chosen too large, the original DFT wave functions are not well reproduced near the matching plane (where the intrinsic noise is small).

The values $\psi(\mathbf{k}, z_{\text{start}}(\mathbf{k})) = \psi_{\text{start}}(\mathbf{k})$ are used as the initial conditions for the generalized Numerov integration. They fully determine the shape of the wave function inside region II. For initializing the previous value we use 1D Numerov to estimate $\psi(\mathbf{k}, z_{\text{start}}(\mathbf{k}) - h)$. Similarly, we use 1D Numerov to extend ψ beyond the filtering boundary in an approximate way namely ignoring the effect of in-plane scattering due to the in-plane potential variant ions δV.

In this way, the iso-magnitude contour is effectively treated as our dividing boundary between region I and region II in mixed space. At this boundary, we initialize the Fourier components for the region II integration. In short only coefficients inside the boundary are included in the generalized Numerov for region II. Outside this contour boundary, i.e., in region I, we rescale the precomputed 1D Numerov solutions to match the boundary value.

We note in passing that we can combine the iso-magnitude boundary condition with a maximum for z_{start} based on the in-plane lateral variations δV. In such a case, we cap the contour when the lateral variations become negligible, and thus the 1D Numerov integration is accurate (and far more efficient).

4. *Fourier filtered generalized Numerov*

To summarize the Fourier-filtered generalized Numerov, the iteration proceeds as follows:

(1) Given $\psi(\mathbf{k}, z_{n-1})$ in mixed space and $\psi(x, y, z_n)$ in real space on a regular discretization grid, Fourier transforms the latter one to mixed space via fast Fourier transforms (FFT).
(2) Set $\psi(\mathbf{k}, z_n) := 0$ where $z_n > z_{\text{start}}(\mathbf{k})$.
(3) For cases at the boundary, where $z_n = z_{\text{start}}$, set

$$\psi(\mathbf{k}, z_n) = \psi_{\text{start}}(\mathbf{k}),$$
$$\psi(\mathbf{k}, z_{n-1}) = \psi_{\text{start}}(\mathbf{k}) \cdot \frac{\psi_{1d}(\mathbf{k}, z_{n-1})}{\psi_{1d}(\mathbf{k}, z_n)}.$$

(4) Save $\psi(\mathbf{k}, z_n)$ for the next iteration.
(5) Fourier transform both $\psi(\mathbf{k}, z_{n-1})$ and $\psi(\mathbf{k}, z_n)$ to real space.
(6) Perform generalized Numerov propagation by solving Eq. (13), yielding the real space for the next iteration z_{n+1}.

When z_{match} has been reached, the missing region I tails are added to the mixed-space representation by setting

$$\psi(\mathbf{k}, z_n) = \psi_{\text{start}}(\mathbf{k}) \cdot \frac{\psi_{1d}(\mathbf{k}, z_n)}{\psi_{1d}(\mathbf{k}, z_{\text{start}}(\mathbf{k}))} \tag{15}$$

for all $z_n > z_{\text{start}}(\mathbf{k})$. Afterward, the real-space representation can be recomputed from this via in-plane FFTs.

E. Iterative determination of ψ_{start}

The final step is to determine the starting values $\psi_{\text{start}}(\mathbf{k})$ such that integration across region II according to the algorithm described above yields values $\psi_{II}(x, y, z_{\text{match}})$ at the matching plane that agree with the desired values. These values are given by the original DFT wave function in region III, i.e., by $\psi_{III}(x, y, z_{\text{match}})$.

For this purpose, we define the residue

$$R(\mathbf{k}) = \psi_{III}(\mathbf{k}, z_{\text{start}}) - \psi_{II}(\mathbf{k}, z_{\text{match}}) \tag{16}$$

that implicitly depends on $\psi_{\text{start}}(\mathbf{k})$, and solve the multidimensional root-finding problem $R = 0$, treating R as a function of ψ_{start}. However, there is a huge difference in magnitude between the residue R (which is similar in scale to the wave function at the matching plane), and the starting values ψ_{start} at the iso-contour boundary. The latter are smaller by a factor η, cf. Eq. (14). To accommodate the scale, we iterate on

$$\psi_{\text{init}}(\mathbf{k}) = \psi(\mathbf{k}) \cdot \frac{\psi_{1d}(\mathbf{k}, z_{\text{match}})}{\psi_{1d}(\mathbf{k}, z_{\text{start}}(\mathbf{k}))}. \tag{17}$$

ψ_{init} can be thought of as the boundary values rescaled to the matching plane via the 1D Numerov approximation. We use this flexible definition rather than the constant η to accommodate situations in which we limit $z_{\text{start}}(\mathbf{k})$ to a maximum based on the magnitude of δV, as explained in Sec. III D 3. The root finding algorithm, of scipy with Krylov iteration and numerical inverse Jacobian estimation [43], is then used to solve for the starting values, completely analogous to our solution of the generalized Numerov propagation, Eq. (13), see Sec. III D 1. Figure 8 illustrates the comparison of the original, noisy wave function from the global DFT solver with one from EXTRA on the log scale. It demonstrates that EXTRA overcomes the limitations of the global solution.

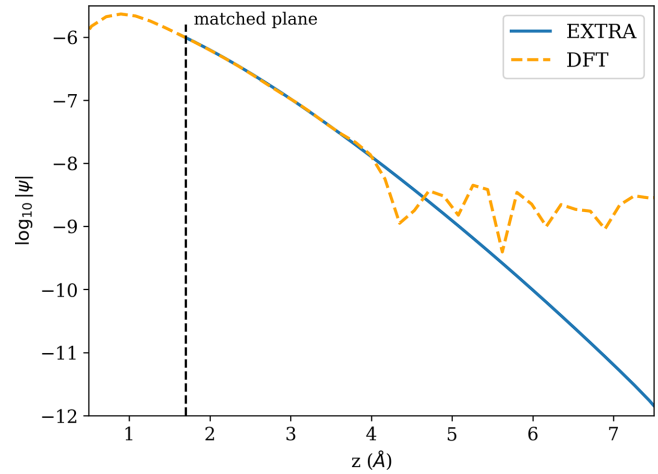

FIG. 8. Comparison of EXTRA and DFT computed wave functions of Ta-Ni(012) along the direction z. The topmost nuclear positions are located at $z = 0$. The wave functions correspond to an eigenvalue at the Fermi level. The position of the matched plane (dashed line) is located at $z_{\text{match}} = 1.7$ Å where both curves have been aligned.

IV. INVESTIGATION OF SUBSTITUTIONAL IMPURITIES IN NI

A. Chemical contrast for Ta in Ni(012)

In this section, we will illustrate that the EXTRA algorithm allows us to overcome the accuracy limitations that prevented direct simulations of FIM contrast. For this evaluation, we choose the case of substitutional Ta in Ni, before we analyze systematic trends for 5d elements series (Ta, W, Re) in Sec. IV C. We have selected these systems because transition metal solutes in Ni have been demonstrated to enhance high-temperature deformation resistance, a critical property for Ni-based superalloys [45]. In a recent aFIM study with Ne as an imaging gas, Morgado *et al.* investigated segregation in Ni alloys with 2% Ta [11]. They observed that Ta was imaged in FIM more brightly than Ni. This finding was qualitatively explained by DFT calculations performed by some of the present authors. The DFT calculations showed that Ta-related states appear energetically at 1–3 eV above the Fermi level, while only a few Ni states in the spin minority channel are available for tunneling electrons up to 1 eV above the Fermi level. However, due to the accuracy limitations, we could not actually compute the FIM contrast at relevant ionization energies, nor verify that Ta-related states at higher energies give at all a brighter signal than the lower-lying Ni states. More recently, Klaes *et al.* [13] provided quantitative data for the spot intensity distribution of the Ni-Ta alloy in FIM. They show two distinct maxima in the intensity histogram of imaged atoms (Ta and Ni) from field ion images, and concluded that intensity can be used to deduce the chemical identity of the imaged atoms with some confidence. We will compare our computed intensity ratios with this experimental data in Sec. IV B.

Figure 9 illustrates the results at a realistic ionization energy of 21.5 eV. In the left plot, we show simulated FIM Image from the original DFT wave functions. At ionization energy

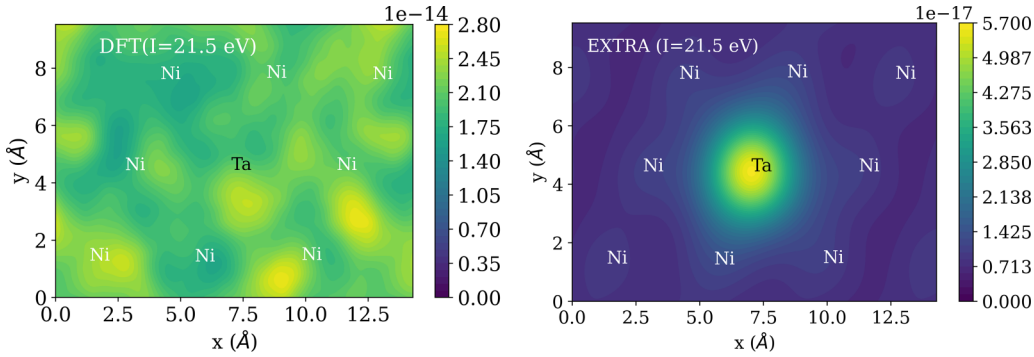

FIG. 9. Simulated FIM images of Ta-Ni(012) for an ionization energy of 21.5 eV. Left: Partial DOS obtained from the original (noisy) DFT wave functions. Right: Refined results from EXTRA. In-plane positions of the top layer atoms are indicated in the graph.

of 21.5 eV, the simulated contrast contains only noise. On the other hand, the results obtained with EXTRA in the right plot show a very clear contrast between Ta and surrounding Ni atoms. As a result, the observed brightness contrast of Ta in Ni shows the effectiveness of our approach, EXTRA.

What happens to noise at a distance closer to the surface? As described in Sec. II, we can treat the ionization energy I as a tunable parameter to evaluate the FIM contrast at different heights. At lower ionization energies of 10 eV and 15 eV, there is a single bright spot arising from Ta even from the raw DFT wave functions (see Supplemental Material [44]). Figure 10 shows line profiles of the simulated FIM intensity at different ionization energies. The line scans run along the x axis across the Ta atom and its two Ni neighbors. The solid lines illustrate the DFT results while EXTRA results are shown by dashed lines. At I = 10 eV and 15 eV, i.e., more closer to the surface, one can not see noise. However, the relative contrast clearly changes at 10 eV and 15 eV. It is concluded that peak shape varies with ionization energy. This highlights that one has to simulate using the correct ionization energy to do a quantitative comparison with the experiment. The comparison of different ionization energies shows that all features become broader with increasing ionization energy (and hence increasing distance from the surface). One can clearly see the intensity difference of five orders in magnitude at I = 10 eV and 21.5 eV, that clearly indicates the stable performance of our algorithm EXTRA over several orders of magnitude. At higher ionization energy of 21.5 eV the noise level from DFT exceeds by two orders of magnitude the expected true signal from EXTRA. The simulated FIM contrast is hence strongly improved by the extrapolation of wave-function tails.

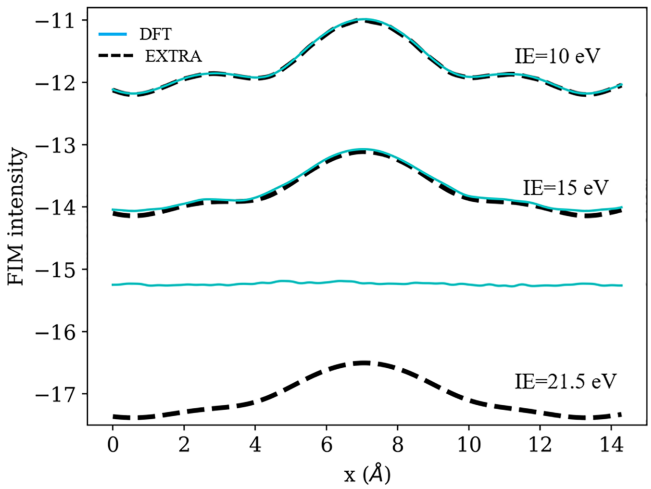

FIG. 10. 1D line scans of the simulated FIM intensity from Fig. 9 on a log scale. The line runs along the x axis across the Ta position.

B. Comparison to experiment

Klaes *et al.* [13] studied a NiTa alloy using 3D-FIM. Using two-pass algorithm [17] they have analysed the intensity spectrum of imaged atoms right before evaporation. Based on their observations, we performed a comparison by calculating the peak intensity of Ni and Ta. Referring to Fig. 4 b of Klaes *et al.* [13], we calculate the peak intensity ratio from intensity distribution. The intensity spectrum runs between 0 and 250 for the corresponding Ni and Ta spots. Ni appears as a broad feature around 44 (FWHM: $\approx$ 50) while Ta feature peaks at 222 (FWHM: $\approx$20). Considering these two different intensities we compute the experimental ratio as $I_{\mathrm{Ta}}/I_{\mathrm{Ni}} = 5.05$. In our current paper, we compare intensity from pure Ni metal and added impurities. From FIM simulation we found the peak intensity ratio to be $I_{Ta}/I_{Ni} = 6.18$. Our theoretical ratio is found to be in reasonable agreement with experimental value, being larger than the experimental observation by 23%.

C. Effect of impurities on contrast

Following the same approach, we have investigated the FIM appearance of tungsten (W) and rhenium (Re) on Ni(012) surface. The FIM contrast maps are similar to the Ta case (Fig. 9) with a single bright spot from the substituted atoms (see Supplemental Material [44]). However, the brightness enhancement varies with the chemical element. To illustrate this, Fig. 11 provides the FIM intensity profiles for Ta, W, and Re substitution along a line running through the central atom and its Ni neighbors along the x direction. For reference, we included the case of a pure Ni surface. The comparison shows that the maximum enhancement in contrast is for the Ta atom and Re shows the minimum, i.e., Ta > W > Re. From the line profile plots, we can extract the relative peak intensities of these elements. For the case of tungsten it is $I_W/I_{Ni} = 5.06$ and for Re $I_{Re}/I_{Ni} = 4.38$.

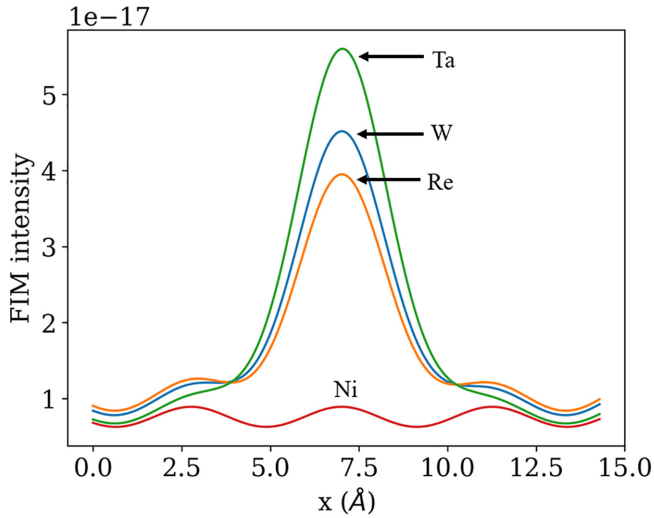

FIG. 11. 1D line scans of the simulated FIM intensity for Ta, W, and Re on Ni(012) running along the x axis (horizontally see Fig. 9) across the central atom. The red curve shows the FIM intensity for pure Ni.

The enhanced brightness of 5d elements emerges from the underlying electronic structure. To analyze the surface electronic structure atom by atom, we projected the density of states inside spheres around each surface atom. The atomic-projected DOS plots shown in Fig. 12 qualitatively explain the electronic effect. Ni contains an almost filled d band. Tunneling into Ni d-states is possible only for a small unoccupied fraction above the Fermi level. All three elements Ta, W, and Re exhibit a very significant local density of unoccupied d orbitals above the Fermi level. Going from Ta $\rightarrow$ W $\rightarrow$ Re (increased d filling), the empty states decrease in number and shift to lower energies. Interestingly, the former effect seems to overcompensate the expected damping of tunneling into the higher-lying states, as explained in Sec. II. Therefore brightness contrast is dominated by the available unoccupied DOS

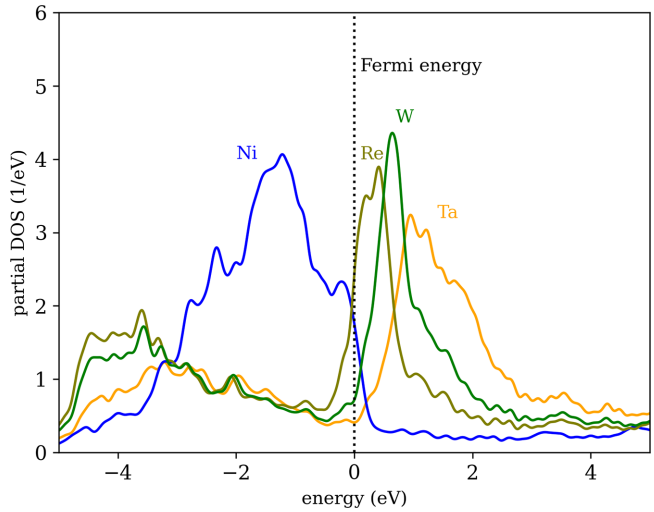

FIG. 12. Atom-projected density of states for W, Ta, and Re atoms located in the top surface layer of Ni(012). Fermi energy is referred at zero.

as speculated in our previous paper for Ta in Ni(012) [11]. Tunneling into these orbitals will enhance the local ionization probability and hence the FIM brightness.

V. CONCLUSIONS

In this paper, we have laid out the foundations for an accurate computation of tunneling-related contrast in field ion microscopy based on state-of-the-art density functional theory. For this, we apply the Tersoff-Hamann approximation known from scanning tunneling microscopy to the characteristic situation of tunneling into imaging gas atoms hovering above the surface in the presence of a very strong field. We identified the numerical accuracy of wave functions from the global solvers employed in plane wave DFT codes as a major limitation, and developed an algorithm, termed EXTRA, to recompute these tails in a very robust manner over many orders of magnitude. Equipped with this algorithm, we demonstrate for a prototypical case, Ta in Ni, that we can simulate FIM contrast maps at realistic ionization energies with practically no noise. This scheme paves the way to systematically address open questions of contrast generation in FIM. We note that the applicability of the EXTRA algorithm is not limited to these cases but may be employed for other surface science questions where the tails of the wave functions are of interest, e.g., in overcoming tail shape limitations when localized orbitals are used as a basis set. See the Supplemental Material [44] for spin-resolved atom projected partial density of states for all three elements.

The code is available on github [46].

ACKNOWLEDGMENTS

The authors like to thank Felipe M. Morgado and Baptiste Gault for their valuable discussions. We further thank the pyiron developers, notably Marvin Poul, for their continuous technical support. S.B. gratefully acknowledges financial support from the International Max Planck Research School for Sustainable Metallurgy (IMPRS SusMet).

APPENDIX A: ELECTROSTATIC POTENTIAL COMPUTED VIA POISSON EQUATION

The second derivative of the electrostatic potential relates to the local charge density in Poisson's equation

$$\nabla^2\phi(\mathbf{r}) = -\frac{\rho(\mathbf{r})}{\epsilon_0}. \tag{A1}$$

If in-plane Fourier transform is applied along with periodic boundary conditions denoted by (k_x, k_y) where $k = \sqrt{k_x^2 + k_y^2}$ and perpendicular to z, Eq. (A1) becomes separable as

$$\frac{\partial^2}{\partial z^2}V(k_x, k_y, z) = |\mathbf{k}|^2 V(k_x, k_y, z) - \frac{\rho(k_x, ky, z)}{\epsilon_0}. \tag{A2}$$

The solution in the charge-free region is

(i) if $|\mathbf{k}| = 0$

$$V(kx = 0, ky = 0, z) = D + E_z z \tag{A3}$$

for constant electric field E_z, and

(ii) if $|\mathbf{k}| > 0$

$$V(k_x, k_y, z) = D + C_1 e^{-|\mathbf{k}|z} + C_2 e^{|\mathbf{k}|z}. \tag{A4}$$

Of course, any nonzero potential variation must be matched by charges on the counter electrode. For an ideal metallic plate-like counter electrode far away, only a homogeneous surface charge is possible that accommodates the average field E_z. Therefore, only the decaying solution $e^{-|\mathbf{k}|z}$ must be considered for $|\mathbf{k}| > 0$.

APPENDIX B: DERIVATION OF THE GENERALIZED NUMEROV ALGORITHM

The Kohn-Sham equation in three dimensions can be expressed as

$$\frac{1}{2}\frac{\partial^2}{\partial z^2}\psi(\mathbf{x}, z) + \{\epsilon - \hat{V}(z)\}\psi(\mathbf{x}, z) = 0 \tag{B1}$$

with the in-plane operator

$$\hat{V}(z) = -\frac{1}{2}\left(\frac{\partial^2}{\partial x^2} + \frac{\partial^2}{\partial y^2}\right) + V(\mathbf{x}, z). \tag{B2}$$

$\mathbf{x}$ comprises the in-plane coordinates in either real or mixed space. The in-plane operator is strictly local along the z direction, but within the plane, it is semilocal (in real space) or even nonlocal (in mixed space). Next, we discretize along the z direction with a spacing h, i.e., $z_n = nh$, and Taylor series expansion of ψ to fifth order [with $\psi_n = \psi(\mathbf{x}, z_n)$],

$$\begin{aligned}\psi_{n\pm1} = \psi_n &\pm h\frac{\partial}{\partial z}\psi_n + \frac{h^2}{2}\frac{\partial^2}{\partial z^2}\psi_n \\ &\pm \frac{h^3}{6}\frac{\partial^3}{\partial z^3}\psi_n + \frac{h^4}{24}\frac{\partial^4}{\partial z^4}\psi_n \\ &\pm \frac{h^5}{120}\frac{\partial^5}{\partial z^5}\psi_n + \mathcal{O}(h^6).\end{aligned} \tag{B3}$$

Adding the equations for ψ_{n+1} and ψ_{n-1} makes the odd derivatives vanish. To evaluate the term involving the fourth derivative we act on Eq. (B1) with $1 + \frac{h^2}{12}\frac{\partial^2}{\partial z^2}$, which gives

$$\frac{\partial^2}{\partial z^2}\psi_n + \frac{h^2}{12}\frac{\partial^4}{\partial z^4}\psi_n + \{\epsilon - \hat{V}(z)\}\psi_n + \frac{h^2}{12}\frac{\partial^2}{\partial z^2}\{\epsilon - \hat{V}(z)\}\psi_n = 0. \tag{B4}$$

Substituting for $\frac{\partial^2}{\partial z^2}\psi_n + \frac{h^2}{12}\frac{\partial^4}{\partial z^4}\psi_n$ and evaluate $\frac{\partial^2}{\partial z^2}\{\epsilon - \hat{V}(z)\}\psi_n$ gives

$$\frac{\partial^2}{\partial z^2}\{\epsilon - \hat{V}(z_n)\}\psi_n = \frac{\{\epsilon - \hat{V}(z_{n+1})\}\psi_{n+1} + \{\epsilon - \hat{V}(z_{n-1})\}\psi_{n-1} - 2\{\epsilon - \hat{V}(z_n)\}\psi_n}{h^2}. \tag{B5}$$

With this substitution, one can rearrange terms to arrive at

$$\left[1 + \frac{1}{6}h^2\{\epsilon - \hat{V}(z_{n+1})\}\right]\psi_{n+1} = 2\left[1 - \frac{5}{6}h^2\{\epsilon - \hat{V}(z_n)\}\right]\psi_n - \left[1 + \frac{1}{6}h^2\{\epsilon - \hat{V}(z_{n-1})\}\right]\psi_{n-1}. \tag{B6}$$

[1] E. W. Müller, Das Feldionenmikroskop, Z. Phys. **131**, 136 (1951).

[2] E. W. Müller, Resolution of the atomic structure of a metal surface by the field ion microscope, J. Appl. Phys. **27**, 474 (1956).

[3] D. Brandon, The resolution of atomic structure: Recent advances in the theory and development of the field ion microscope, Br. J. Appl. Phys. **14**, 474 (1963).

[4] J. Chen, *Introduction to Scanning Tunneling Microscopy Third Edition* Vol. 69 (Oxford University Press, New York, 2021).

[5] A.-S. Lucier, H. Mortensen, Y. Sun, and P. Grütter, Determination of the atomic structure of scanning probe microscopy tungsten tips by field ion microscopy, Phys. Rev. B **72**, 235420 (2005).

[6] S. Katnagallu, F. F. Morgado, I. Mouton, B. Gault, and L. T. Stephenson, Three-dimensional atomically resolved analytical imaging with a field ion microscope, Microsc. Microanal. **28**, 1264 (2022).

[7] F. Vurpillot, M. Gilbert, and B. Deconihout, Towards the three-dimensional field ion microscope, Surf. Interface Anal. **39**, 273 (2007).

[8] M. Dagan, B. Gault, G. D. Smith, P. A. Bagot, and M. P. Moody, Automated atom-by-atom three-dimensional (3D) reconstruction of field ion microscopy data, Microsc. Microanal. **23**, 255 (2017).

[9] B. Klaes, R. Larde, F. Delaroche, S. Parviainen, N. Rolland, S. Katnagallu, B. Gault, and F. Vurpillot, A model to predict image formation in the three-dimensional field ion microscope, Comput. Phys. Commun. **260**, 107317 (2021).

[10] S. Katnagallu, L. T. Stephenson, I. Mouton, C. Freysoldt, A. P. Subramanyam, J. Jenke, A. N. Ladines, S. Neumeier, T. Hammerschmidt, R. Drautz *et al.*, Imaging individual solute atoms at crystalline imperfections in metals, New J. Phys. **21**, 123020 (2019).

[11] F. F. Morgado, S. Katnagallu, C. Freysoldt, B. Klaes, F. Vurpillot, J. Neugebauer, D. Raabe, S. Neumeier, B. Gault, and L. T. Stephenson, Revealing atomic-scale vacancy-solute interaction in nickel, Scr. Mater. **203**, 114036 (2021).

[12] M. Scott, C.-C. Chen, M. Mecklenburg, C. Zhu, R. Xu, P. Ercius, U. Dahmen, B. Regan, and J. Miao, Electron tomography at 2.4-ångström resolution, Nature (London) **483**, 444 (2012).

[13] B. Klaes, J. Renaux, R. Lardé, F. Delaroche, F. F. Morgado, L. T. Stephenson, B. Gault, and F. Vurpillot, Analytical three-dimensional field ion microscopy of an amorphous glass FeBSi, Microsc. Microanal. **28**, 1280 (2022).

[14] J. O. de Beeck, C. Freysoldt, R. Cuduvally, J. Scheerder, R. J. Morris, P. van der Heide, W. Vandervorst, and C. Fleischmann, Evaporation dynamics of boron dopants in silicon, Microsc. Microanal. **27**, 418 (2021).

[15] C. Speicher, W. Pimbley, M. Attardo, J. Galligan, and S. Brenner, Observation of vacancies in the field-ion microscope, Phys. Lett. **23**, 194 (1966).

[16] J. Park, H. Huang, R. Siegel, and R. Balluffi, A quantitative study of vacancy defects in quenched tungsten by combined field-ion microscopy and electrical resistometry, Philos. Mag. A **48**, 397 (1983).

[17] B. Klaes, R. Lardé, F. Delaroche, C. Hatzoglou, S. Parvianien, J. Houard, G. Da Costa, A. Normand, M. Brault, B. Radiguet *et al.*, Development of wide field of view three-dimensional field ion microscopy and high-fidelity reconstruction algorithms to the study of defects in nuclear materials, Microsc. Microanal. **27**, 365 (2021).

[18] Y. Suchorski, I. Bespalov, J. Zeininger, M. Raab, M. Datler, P. Winkler, and G. Rupprechter, Co oxidation on stepped rh surfaces: µm-scale versus nanoscale, Catal. Lett. **150**, 605 (2020).

[19] S. Katnagallu, M. Dagan, S. Parviainen, A. Nematollahi, B. Grabowski, P. A. J. Bagot, N. Rolland, J. Neugebauer, D. Raabe, F. Vurpillot, M. P. Moody, and B. Gault, Impact of local electrostatic field rearrangement on field ionization, J. Phys. D: Appl. Phys. **51**, 105601 (2018).

[20] R. G. Forbes, Field-ion image formation, Nat. Phys. Sci. **230**, 165 (1971).

[21] R. G. Forbes, A theory of field-ion imaging: I. A quasi-classical site-current formula, J. Microsc. **96**, 57 (1972).

[22] R. G. Forbes, A theory of field-ion imaging: II. On the origin of site-current variations, J. Microsc. **96**, 63 (1972).

[23] R. Haydock and D. R. Kingham, Field ionization theory: A new, analytic, formalism, Surf. Sci. **103**, 239 (1981).

[24] R. G. Forbes, Seeing atoms: The origins of local contrast in field-ion images, J. Phys. D **18**, 973 (1985).

[25] S. Lam and R. Needs, Field-ion microscope tunnelling calculations for the aluminium (111) and (110) surfaces, Surf. Sci. **277**, 173 (1992).

[26] S. Lam and R. Needs, Theory of field ionization, Appl. Surf. Sci. **76-77**, 61 (1994).

[27] R. G. Forbes, Field electron and ion emission from charged surfaces: A strategic historical review of theoretical concepts, Ultramicroscopy **95**, 1 (2003).

[28] F. Vurpillot, A. Bostel, and D. Blavette, A new approach to the interpretation of atom probe field-ion microscopy images, Ultramicroscopy **89**, 137 (2001).

[29] S. S. Katnagallu, On chemically sensitive atomic scale imaging, doctoralthesis, Ruhr-Universität Bochum, Universitätsbibliothek, 2018.

[30] J. Tersoff and D. R. Hamann, Theory of the scanning tunneling microscope, Phys. Rev. B **31**, 805 (1985).

[31] M. C. Payne, M. P. Teter, D. C. Allan, T. Arias, and a. J. Joannopoulos, Iterative minimization techniques for ab initio total-energy calculations: Molecular dynamics and conjugate gradients, Rev. Mod. Phys. **64**, 1045 (1992).

[32] S. Boeck, C. Freysoldt, A. Dick, L. Ismer, and J. Neugebauer, The object-oriented DFT program library s/phi/nx, Comput. Phys. Commun. **182**, 543 (2011).

[33] J. P. Perdew, K. Burke, and M. Ernzerhof, Generalized Gradient Approximation Made Simple, Phys. Rev. Lett. **77**, 3865 (1996).

[34] C. Freysoldt, A. Mishra, M. Ashton, and J. Neugebauer, Generalized dipole correction for charged surfaces in the repeated-slab approach, Phys. Rev. B **102**, 045403 (2020).

[35] C. Freysoldt, On-the-fly parameterization of internal coordinate force constants for quasi-newton geometry optimization in atomistic calculations, Comput. Mater. Sci. **133**, 71 (2017).

[36] D. Sholl and J. A. Steckel, *Density Functional Theory: A Practical Introduction* (John Wiley & Sons, Hoboken, NJ, 2011).

[37] M. Purevkhuu and V. Korobov, On one implementation of the Numerov method for the one-dimensional stationary Schrödinger equation, Phys. Part. Nucl. Lett. **18**, 153 (2021).

[38] D. Bennett, Numerical solution of time-independent 1-D Schrödinger equation (2015), https://www.maths.tcd.ie/~dbennett/js/schro.pdf.

[39] A. Raptis and A. C. Allison, Exponential-fitting methods for the numerical solution of the Schrodinger equation, Comput. Phys. Commun. **14**, 1 (1978).

[40] T. Simos, A new Numerov-type method for the numerical solution of the Schrödinger equation, J. Math. Chem. **46**, 981 (2009).

[41] M. Pillai, J. Goglio, and T. G. Walker, Matrix Numerov method for solving Schrödinger's equation, Am. J. Phys. **80**, 1017 (2012).

[42] P. Virtanen, R. Gommers, T. E. Oliphant, M. Haberland, T. Reddy, D. Cournapeau, E. Burovski, P. Peterson, W. Weckesser, J. Bright *et al.*, Scipy 1.0: Fundamental algorithms for scientific computing in python, Nat. Methods **17**, 261 (2020).

[43] C. T. Kelley, *Iterative Methods for Linear and Nonlinear Equations* (SIAM, Philadelphia, 1995).

[44] See Supplemental Material at http://link.aps.org/supplemental/10.1103/PhysRevB.107.235413 for outcomes from unfiltered generalized Numerov; FIM images from raw DFT and EXTRA of Ta, W, and Re in Ni(012); atom projected DOS plots.

[45] H. ur Rehman, K. Durst, S. Neumeier, A. Sato, R. Reed, and M. Göken, On the temperature dependent strengthening of nickel by transition metal solutes, Acta Mater. **137**, 54 (2017).

[46] https://github.com/eisenforschung/EXTRA_FIM.git.